ChemElectroChem

Research Article
doi.org/10.1002/celc.202500098

Chemistry Europe
European Chemical Societies Publishing

www.chemelectrochem.org

Tracing Iridium Dissolution Pathways in Proton Exchange Membrane Water Electrolyzers at Relevant Current Densities in Real Time

Nico C. Röttcher,* Jiahua Zhou, Lukas Löttert, Karl J. J. Mayrhofer, and Dominik Dworschak*

Catalyst dissolution is one of the key challenges in achieving long-term performance in proton exchange membrane water electrolysis with low iridium loading. However, most of the dissolved catalyst remains in the catalyst-coated membrane, inaccessible for operando quantification. While simpler aqueous model systems improve mechanistic understanding, dissolution rates are significantly overestimated compared to the device level. To bridge this gap, herein, an electrochemical half-cell setup that mimics the anode catalyst layer environment to enable operation at relevant current densities ($>1\ A\ cm^{-1}$) is presented. Dissolved catalyst species transported through the porous transport layer or through the membrane are separately detected operando by coupling to inductively coupled plasma-mass spectrometry. The results demonstrate a strong preference for the transport of dissolved iridium through the membrane (99.9%) and a decrease in catalyst stability by factor 10 at high current densities. Discrepancies with so far reported findings from full-cell and half-cell experiments highlight a lack of understanding of catalyst dissolution and the transportation of dissolved species in different systems. The presented method offers unique insights which will help to study and optimize catalyst dissolution by means of various manufacturing and operation parameters to ultimately improve the stability of catalyst layers for water electrolysis.

1. Introduction

Proton exchange membrane water electrolysis (PEMWE) is emerging as a key technology for the energy transition toward net-zero emissions.[1] A critical parameter to enable its widespread application is a reduction in the loading of iridium in the anode catalyst layer (ACL) due to its price and availability.[2–5] In recent years, there has been significant progress in enabling high activity using low-loaded ACLs.[6–9] However, ensuring long-term stability with these electrodes remains challenging. With a decrease in loading, mechanisms that result in a loss of active catalyst, such as catalyst dissolution, are significant.[10,11] To quantify the effect of catalyst dissolution, electrochemical performance parameters are insufficient due to i) the low sensitivity of the potential on catalyst dissolution and ii) the need to decouple a variety of other degradation mechanisms from individual components of an electrolyzer, such as the bipolar plate, the porous transport layers (PTLs), the catalyst layers (CLs), and the proton exchange membrane (PEM), as well as their interfaces.[12–14] In contrast, complementary techniques such as inductively coupled plasma-mass spectrometry (ICP-MS) enable the quantification of dissolved catalyst within a liquid stream with a resolution down to the second.[15,16] In full-cell electrolyzer, dissolved iridium was quantified in the anode and cathode water line.[17] A comparison with a post-mortem analysis of the catalyst-coated membrane (CCM) revealed that a significant amount (>90%) of dissolved iridium redeposits in the CCM, remaining inaccessible for in operando detection.[17]

To quantify the amount of dissolved iridium during operation, Dam et al. proposed a procedure based on the observation that iridium dissolves as anionic and cationic species.[18] Determining their ratio in the anode water feed enables an estimation of the distribution of sinks on the PTL or membrane side and, by this, the total dissolution rate. This procedure, however, relies on the assumption of i) a constant ratio of 80/20 between the iridium species dissolved as cations or anions and ii) the exclusive transport of the anionic species through the PTL. Under constant operation, the authors estimated that 72% of the dissolved catalyst remains in the CCM.[18]

As illustrated in **Figure 1**A, the distribution of the dissolved catalyst between the two pathways is the result of the interaction of the intrinsic dissolution process, the transport of dissolved species toward the PTL or cathode, and the sinks of dissolved species, i.e., the removal through the water lines, the formation of an Ir band in the membrane in close proximity to the anode, as well as the electrochemically driven redeposition in the cathode catalyst layer (CCL).[10,17,19] Depending on the transport and sink rate,

N. C. Röttcher, J. Zhou, L. Löttert, K. J. J. Mayrhofer, D. Dworschak
Helmholtz Institute Erlangen-Nürnberg for Renewable Energy (IET-2)
Forschungszentrum Jülich
Cauerstr. 1, 91058 Erlangen, Germany
E-mail: n.roettcher@fz-juelich.de
d.dworschak@fz-juelich.de

N. C. Röttcher, J. Zhou, L. Löttert, K. J. J. Mayrhofer
Department of Chemical and Biological Engineering
Friedrich-Alexander-Universität Erlangen-Nürnberg
Cauerstr. 1, 91058 Erlangen, Germany

Supporting information for this article is available on the WWW under https://doi.org/10.1002/celc.202500098

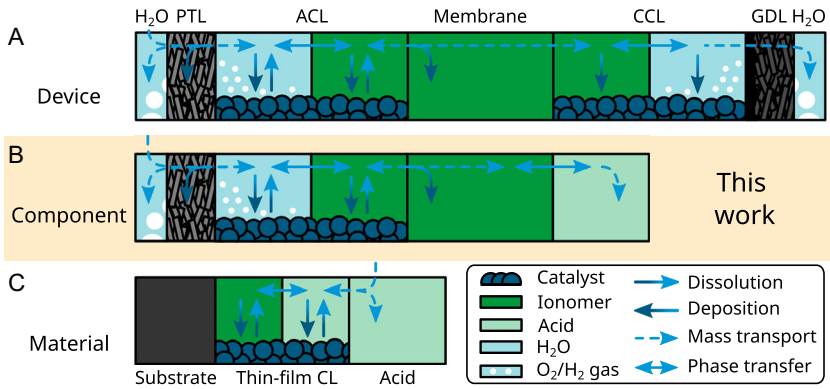

Figure 1. Transport model for dissolved iridium species in different setups: A) device-level research in full-cells;[17,18,29] B) component-level research in half-cell setups for catalyst layer characterization, such as GDE[28] and this work; and C) material-level research in half-cell setups for catalyst thin-film characterization such as SFC[23,26] and RDE.[20]

the concentration of dissolved catalyst within the catalyst layer can be affected and, consequently, the dissolution rate changes in accordance with the Nernst equation.[20,21] The possibility of two pathways and multiple sinks for the dissolved catalyst species in device-level experiments therefore not only hinders the detection of the dissolved catalyst but can also affect the stability of the electrode.

To isolate the intrinsic dissolution process on a material level, experiments in aqueous model systems (AMSs) have been designed with catalyst thin-film electrodes coated on different substrate materials placed in an acidic electrolyte (see Figure 1C).[15,16,22] Using forced convection by rotation in a rotating disk electrode (RDE) or a constant flow in a scanning flow cell (SFC), the transport of dissolved species away from the electrode is enhanced, thus minimizing the redeposition of the catalyst. With the electrolyte being the only sink, the amount of dissolved catalyst can be determined with less effort compared to device-level experiments. For Ir-based catalysts, a proportional increase in the dissolution rate with current density was observed.[23] Based on this finding, Kasian et al. proposed an inherent link between the oxygen evolution reaction (OER) and iridium dissolution by a common intermediate.[24] To compare the stability of different Ir-based catalysts, the stability number (*S*-number) was introduced as the ratio between the moles evolved oxygen and the moles of the dissolved catalyst.[23]

While in most studies the measured dissolution signal is linked to the intrinsic dissolution rate of the material, in some studies, transport effects have been used to explain the trends observed in catalyst dissolution. In RDE experiments, it was shown for Ru- and W-based catalysts that an increase in the concentration of dissolved species in the electrolyte reduced the overall catalyst dissolution rate by shifting the dissolution–redeposition equilibrium according to Nernst equation.[20,25] In contrast, for Ir-based catalysts, such an effect was not observed using a SFC, when adding dissolved iridium into the electrolyte stream.[26] However, an influence of the ionomer on the catalyst dissolution was observed, with decreased stability at a low ionomer content.[26] The slow transport of dissolved catalyst species through the ionomer can increase the concentration of dissolved species at the surface of the catalyst, thus inhibiting further dissolution.[27]

The comparison of the results from material and device level demonstrates a significantly higher stability of Ir-based catalysts in the device level with an at least two orders of magnitude higher *S*-number.[26,28] Several differences in the experimental conditions have been put forward to explain the limited transferability. Increased dissolution on the material level can result from particle detachment due to substrate oxidation and a lower pH as a result of direct contact with an acidic electrolyte.[22,26,29–31] For the latter, it was found that a change in pH from 1 to 3 decreases the dissolution rate by a factor of 3.3.[26] Based on this result, the local pH in full-cells is assumed to be less acidic compared to a pH of 1, which is usually used in AMSs.

Another factor is the typically applied measurement time, which is in the order of minutes/hours for material-level studies, while being in the order of days in the case for device-level studies. An increase in the *S*-number by a factor of 4 in the first few hours was observed in RDE experiments.[18] In full-cell experiments, the *S*-number increased by two orders of magnitude over the course of a month.[29] It is argued that the catalyst has sites of different stability: while the most unstable sites are lost at the beginning of operation, more stable sites become more predominant over time. In addition, it was suggested that the formation of an Ir band in the membrane close to the anode could inhibit the transport of dissolved catalyst species through the membrane, thus increasing the concentration in the CL, slowing down dissolution, and contributing to the observed stabilization.[29]

Another difference is the applied geometric current density. With higher current density in device-level experiments, the production of gas bubbles is higher. Vigorous bubbling of produced oxygen is expected to lead to fast intermixing and thus increased transport of dissolved species through the PTL.[29] In contrast, gas bubbles are blocking transport paths for dissolved species, which impedes transport through the PTL and could increase the concentration of dissolved species in the CL. Whether the latter effect dominates and contributes to the improved stability in device-level experiments has not been studied to the best of the authors' knowledge.

Despite the variety of explanations offered, results from material-level experiments have so far not been directly transferable

to the device level. Further insights are needed into how the stability of catalysts is dependent on the catalyst environment, the duration of the experiment, and the transport of dissolved species.

An intermediate type of setup was introduced to study CLs on a component level, inspired by previous work on ORR fuel cell electrodes known as gas diffusion electrode (GDE) setups (see Figure 1B).[32–35] CLs as used in full-cells with an iridium loading of ≈1 mg_{Ir} cm^{-2} can be studied at relevant current densities >1 A cm^{-2}, while the working electrode (WE) is separated from the counter electrode (CE) by liquid electrolyte and the potential of the former is determined using a reference electrode (RE). While these setups have primarily been used to study the activity of different catalysts,[33,36] Geuß et al. also studied the dissolution of iridium catalysts.[28] As illustrated in Figure 1B, the distribution between the two transport pathways, through the PTL and the membrane, could also be determined.[28] However, dissolution studies in such GDE cells rely on: i) batchwise determination of dissolution products due to continuous redeposition of dissolved catalyst onto the CE, ii) the measurement of CLs deposited on the PTL—porous transport electrodes (PTE)—in contrary CCMs used in state-of-the-art electrolyzers,[37] and iii) a long duration for cell assembly.

Similar to advancements in studying ORR catalyst dissolution in a high-throughput fashion using a scanning gas diffusion electrode (S-GDE),[38] in this work we present an electrochemical setup online-coupled to ICP-MS to study catalyst dissolution during OER operation at relevant current densities. The setup is optimized: i) to prevent redeposition of the dissolved catalyst at the CE, ii) to use half-side coated CCMs (h-CCMs) with typical PEMWE anode loading, and iii) for a quick exchange of samples. With this setup, we study the distribution of dissolved iridium between the PTL and the membrane pathway. Furthermore, we investigate the stability of Ir-based CLs in relation to OER current density and catalyst loading.

2. Results and Discussion

2.1. Design Considerations

In **Figure 2**, the electrochemical set-up used throughout this work is presented. The h-CCM is sandwiched between the PTL connected to the anode water feed and the membrane side facing a flow cell with a liquid electrolyte. By coupling the liquid streams to ICP-MS, the amount of dissolved catalyst transported through the PTL or the membrane can be determined with a resolution down to the second.[15] The analysis of dissolution products is not limited to the catalyst, but also elements used as support, PTL core or coating material can be traced.[39] For the design, the following challenges had to be considered: i) preventing the redeposition of the dissolved catalyst;[17,28] ii) enabling high current density, i.e., bubble removal, electrolyte resistance, and heat management; iii) reducing acidification of the anode line to reduce its effects on dissolution;[26,33] iv) ensuring sufficient electrical contact of the catalyst layer with the PTL; and v) enabling a quick sample exchange.

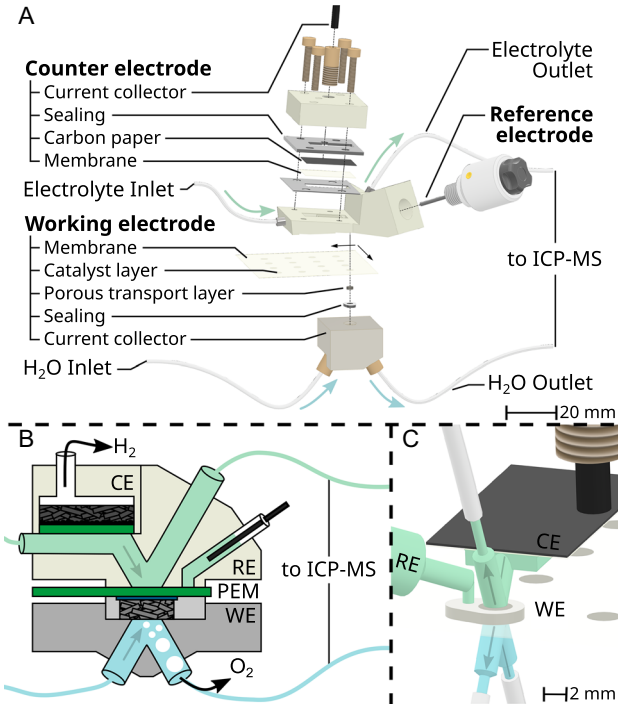

Figure 2. Illustration of the electrochemical setup used in this study. The flow of acidic electrolyte between the electrodes (green) and the flow of water at the back of the WE (blue) are depicted. A) Exploded view of the three-electrode cell. Detailed descriptions of the parts can be found in the Experimental section. B) Schematic of the assembled setup with adjusted sizes of the parts for better visibility. C) Detailed view of the flow channels around the WE and CE, and the separate channel for the RE, which is ionically connected to the WE via the membrane. Cell parts are hidden for better visibility.

The following design choices were therefore made: i) The CE is separated by a liquid electrolyte from the WE and positioned upstream. A continuous flow in the electrolyte compartment prevents the redeposition of the dissolved anode catalyst (see Supplementary Note 1, Supporting Information). A deposition of the dissolved catalyst within the membrane is usually observed in the form of an Ir band in close proximity to the ACL and explained by chemical reduction of the dissolved iridium species by crossover H_2.[13,28,40] With the separation of the CE and the WE, the concentration of H_2 in the membrane is also assumed to be reduced, considering the low solubility of H_2 in aqueous electrolyte.[41] In previous studies using a GDE setup, the formation of an Ir band was not observed for an experiment duration of several hours.[28] Thus, for this study, we assume that iridium redeposition occurs only in negligible amounts. Moreover, a noble-metal-free CE is used to prevent the dissolution of a CE catalyst from interfering with the activity or stability of the WE. For the same reason, a PTL without a noble metal coating is used.

ii) Ionic conductivity between the WE and the CE requires an acidic electrolyte in the upper compartment. However, the introduction of acid in half-cells compared to full-cells is one of the main parameters preventing the translation of results from the material/component level to the device level.[26] The addition of a membrane on the contact area between the electrolyte

and the water compartment, however, significantly reduces the crossover of acid into the anode water line by excluding the counter anion of the acid.[42,43] A recent study by Ngo et al. on acid permeability through Nafion membranes revealed that acid crossover can be minimized by using 1) a low concentration of acid in the electrolyte compartment, 2) a single-pass flow configuration in the anode water compartment without recirculation, and 3) a high flow rate per area of membrane.[42] For the presented setup with a 0.2 M $HClO_4$ electrolyte and an anode water flow rate of 0.75 μL min^{-1}, an acid concentration in the anode water line outlet of pH = 6 can be derived using a simple diffusion model and assuming ideal intermixing in anode compartment (see Supplementary Note 2, Supporting Information). Measurements in the inlet and outlet showed no significant difference in pH. In contrast, in the GDE half-cell setup previously used by Geuß et al. without recirculation and a comparably low volume per membrane area, a significant increase in acid concentration was observed over time in the anode water compartment to a pH of 3.5.[33] The same value can be determined using the diffusion model (see Table S2, Supporting Information).

iii) For high-current operation, a low electrolyte concentration is challenging, as a higher resistance between the WE and CE leads to electrolyte heating and limitations caused by the compliance voltage of the potentiostat. Here, the distance of the CE to the WE is minimized to ≈5 mm, allowing for >1 A cm^{-2} at a compromise electrolyte concentration of 0.2 M $HClO_4$ and reasonably low heating of the electrolyte (see Supplementary Note 3, Supporting Information). While a higher electrolyte concentration would reduce electrolyte heating, a lower concentration compared to previous setups was used to minimize the acidification of the CL and anode water line.[33,34,38]

Furthermore, high-current operation leads to significant bubble formation. To account for this, the CE and the WE are separated from the electrolyte channel by a membrane ensuring the separation of the produced gas to avoid potential disturbances. While this has been observed to be successful for the WE, bubble formation could still be observed in front of the CE at high current densities. In particular, even a single bubble can interfere with the electrochemical measurements (see Figure S1, Supporting Information) due to the small channel diameter (∅ 2 mm).

The membrane on top of the WE also allows for the RE to be connected via the membrane separated from the main electrolyte channel, as previously used in other half-cell[44] and full-cell setups[45,46] (see Figure 2C). The high-frequency resistance (HFR) is thus reduced by about two orders of magnitude compared to a configuration in the main channel. Additionally, the measured potential is not affected by bubbles in the main channel.

iv) Another contributor to the HFR is the CL–PTL interface resistance. The size of the elliptical PTL (∅ 2.5/2.8 mm) is larger compared to the liquid channel opening (∅ 2/2.3 mm). The outer ring of the CL and PTL is thus compressed by the two flow cells, similar to the land parts in full cells. In accordance with full-cell designs, a channel/land ratio of ≈2/1 is chosen.[47] Using pretests with pressure-sensitive paper, the applied force is set to reach a compression of ≈2 MPa at the land (see Figure S2, Supporting Information). The force, however, needs to be adjusted with height differences in the sealing and the PTL. In the channel, in contrast, the CL is not compressed toward the PTL, and swelling of the membrane can lead to creeping into the electrolyte channel. To minimize this effect, a comparably small channel size (∅ 2 mm) is chosen. A smaller channel size is also beneficial considering the material consumption and the temporal resolution of the dissolution signal measured by ICP-MS. The chosen value for the channel diameter is thus a compromise between multiple effects.

v) The diameter of the CL (∅ 3 mm) is even larger than that of the PTL to account for tolerances in the positioning of the sample but is also limited to minimize edge effects and reduce material consumption. A 1 mm-thick PTL is chosen to keep the PTL in place when the two flow cells are moved apart and a new sample is inserted. A quick exchange of the samples is thus ensured, which is a key factor for high-throughput experiments.

Lastly, it should be noted that the potential along the catalyst layer is inhomogeneously distributed due to the upstream position of the CE as well as the inhomogeneous compression distribution. By keeping the sample size small and placing the RE channel orthogonal to the axis between the WE and the CE, the determination of a reasonable averaged potential is assumed. Still, the catalyst at the edge of the PTL with a lower interfacial resistance from the CL to the PTL as well as the catalyst more closely to the CE is more active and the current is expected to be inhomogeneously distributed. The influence of the inhomogeneous current distribution on activity and stability of the catalyst layer is discussed in the following sections.

2.2. Electrochemical Results

Figure 3 displays the electrochemical results of galvanostatic step polarization experiments for CLs containing IrO_2/TiO_2. The potential of each step is corrected for the HFR derived from impedance measurements at each step (see Supplementary Note 6, Supporting Information).

At a low current density (<10 mA cm^{-2}), a reasonable Tafel slope of 56 ± 1 mV dec^{-1} is determined (see Figure 3B), which is comparable to previous half-cell measurements with a PTE using the same catalyst.[33] However, at elevated current densities (>100 mA cm^{-2}), a significant deviation from the linear behavior is observed. This increase in overpotential is explained by the

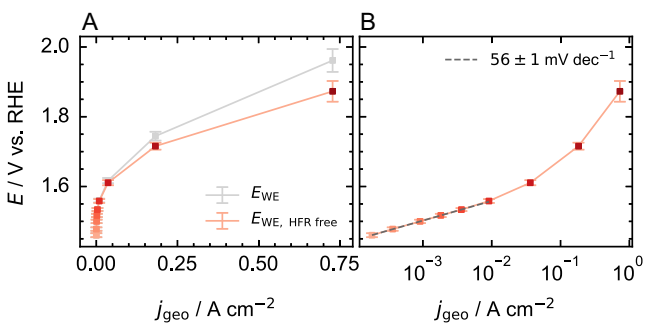

Figure 3. Electrochemical activity characterization displaying the average of three independent measurements: A) polarization curve; B) Tafel representation.

inhomogeneous current distribution as explained before with high current density close to the CE and at the edge of the CL well compressed toward the PTL. Consequently, mass transport limitations due to liquid and gas transport become significant at a lower total current density compared to full-cell experiments.

Similarly, an inhomogeneous current distribution was observed in full cells using a PTL with microstructured pores, mimicking inhomogeneous contact resistance distribution.[48] In-plane swelling of the Nafion membrane and increased gas pressure at high current densities exacerbate this effect by bending the h-CCM toward the electrolyte channel, which further increases the CL–PTL contact resistance in the channel. In contrast, through-plane swelling would reduce the contact resistance. In addition, the application of a PTL with a noble metal coating could reduce contact resistance and, therefore, inhomogeneities in the current distribution. Another approach is the addition of a porous but dimensionally stable interlayer, distributing compression across the CL. While an increase in resistance to the CE must be considered from an electrochemical perspective, such an interlayer would interfere with the dissolution measurement by impeding the transport of dissolved species toward the electrolyte. Moreover, the interlayer could be another sink for the dissolved catalyst and the source of other ions.

2.3. Transport Pathways of the Dissolved Catalyst

During electrochemical operation, the dissolution of iridium is triggered. Dissolved iridium is transported either through the membrane into the liquid electrolyte or through the PTL into the anode water line and is subsequently detected online by ICP-MS. The observed concentration of iridium in the two channels during a conditioning hold is depicted in **Figure 4**.

With the start of OER operation, dissolved iridium species can be detected in both channels. After a sharp increase, the concentration—and with it the mass flow rate of dissolved iridium—decreases steadily and seems to approach a steady-state signal. This dissolution profile is in agreement with experiments in AMSs with SFC-ICPMS on thin-film catalyst spots.[23,26,49] A comparison of the total dissolved mass during the current hold illustrates the strong preference (99.9%) for the transport of dissolved species through the membrane compared to the PTL. The mass flow rate from anode water is so low that the steady-state value is within the detection limit of the ICP-MS (see Figure 4C). Considering the detection limit as the maximum dissolution rate through the PTL pathway, the preference of the membrane is even higher (>99.9%) under steady-state conditions.

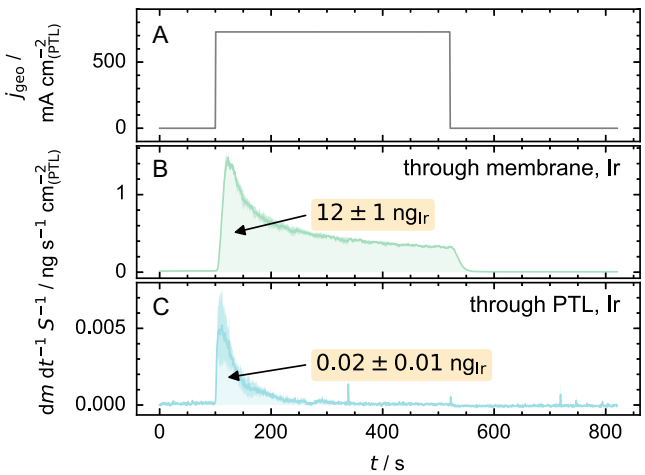

Figure 4. A) Applied current density for electrode conditioning. Dissolution signal of iridium transported B) through the membrane pathway and C) through the PTL during the conditioning for catalyst layers with a loading of 1.7 mg$_{Ir}$ cm^{-2}. The displayed line is the average of two independently measured samples. The darker area displays the minimum and maximum values of the measured samples. Single measurements are displayed in (Figure S1, Supporting Information).

In addition to the difference in steady-state dissolution, further discrepancies in the dissolution profiles of the two transport pathways can be observed and are supported by modeling (see Supplementary Note 7, Supporting Information): i) The delay between the electrochemical and ICP-MS signal and, in turn, the broadening of the dissolution peak is more pronounced for the transport through the membrane compared to the PTL pathway. ii) The stabilization, the decay in concentration, is slower for transport through the membrane compared to the PTL pathway. This trend results in a continuously decreasing ratio between the PTL and the membrane pathway (see Figure S5D, Supporting Information).

A broadening of the peak similar to chromatography experiments usually occurs due to longitudinal diffusion during transport from the electrode to the ICP-MS. The same flow path geometry within the cell, tubing length to the ICP-MS, and flow rate are used for both channels, which means that a significant broadening of the signal is expected to arise from the transport of dissolved iridium through the membrane compared to the pathway through the PTL. Broadening of the signal within the membrane can be explained by a higher share of diffusive transport compared to transport by convection and migration caused by the high concentration gradient from the catalyst layer to the acidic electrolyte ($c_{Ir,aq} \approx 0$) due to the constant flow of fresh electrolyte.[20,27] In contrast, in the PTL, diffusion is less dominant due to a vigorous bubbling of produced oxygen.[29] In terms of the second observation, the faster decay for the PTL pathway, one possible explanation might be a time dependence in the distribution between the two pathways, given a change in temperature and HFR measured during the current hold (see Figure S6, Supporting Information). In addition, assuming that the iridium dissolves as anionic and cationic species, and anionic species are dominant in the PTL pathway, a faster stabilization reaction for the anionic compared to the cationic species might explain the discrepancy in the decay of the two channels.[18]

After the conditioning, dissolution at various current densities is recorded (see Figure S5, Supporting Information). Interestingly, at a low current density (<100 mA cm^{-2}) on the upward sweep, the share of dissolved iridium transported through the PTL increases significantly (>10%), but decreases to the detection limit as soon as higher currents are applied (see Figure S5D, Supporting Information). No increase is observed at a low current density on the backward sweep. As discussed earlier, gas bubbles blocking transport pathways through the PTL at high current

density and continuously during the backward sweep could explain the lower share for the PTL pathway. Another explanation could be the overall proceeding stabilization, as discussed later. These results suggest that the distribution of dissolved iridium between the membrane and the PTL pathway is not only dependent on the operation time within a current hold but also on the applied current density as well as the history of the sample. Within this electrochemical setup and the selected measurement parameters, a strong preference for the membrane pathway is observed.

The same preference for the membrane pathway is found for the dissolution of titanium (see Figure S5E,F, Supporting Information). In the PTL pathway, no significant correlation between the electrochemical protocol and the detection of dissolved titanium species is found. A spiked signal instead indicates particle abrasion. For the membrane pathway, an increase in titanium dissolution with current density is observed but less pronounced compared to iridium. Comparing the dissolved mass of iridium and titanium, especially at a low current density, iridium only accounts for a share of <10 wt% of the total detected dissolved mass (see Figure S5G, Supporting Information). This value could be explained by a disproportionate dissolution of titanium from the catalyst, considering the 75 wt% iridium content. However, as the detected amount of titanium does not change with catalyst loading (see Figure S7, Supporting Information), dissolution from the PTL is more likely. This conclusion, in turn, means that the transport of dissolved titanium into the ionomer phase is so fast that only negligible amounts are washed out into the anode water line.

As depicted in **Figure 5**, in previous reports, the preference for the membrane pathway of dissolved iridium is less pronounced in other electrochemical half- or full-cell setups.[17,18,28] However, the experimental setups and conditions differ significantly.

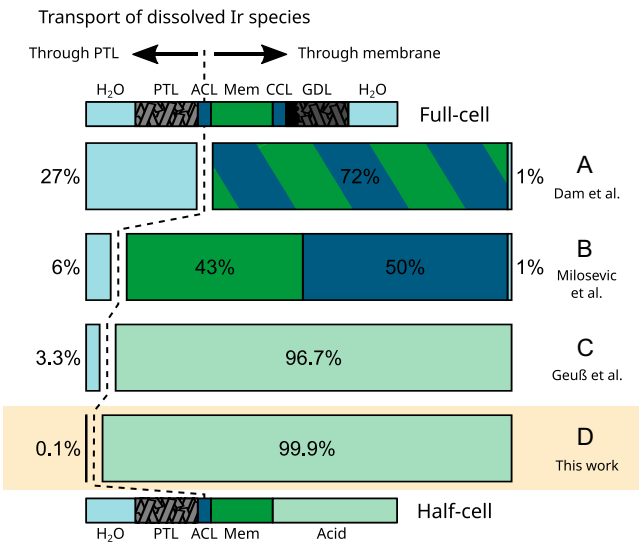

Figure 5. Distribution of dissolved iridium within different electrochemical setups. Setup and experimental details can be found in (Table S6, Supporting Information). Full-cell results: A) Dam et al.[17] B) Milosevic et al.,[18,29] half-cell results: C) Geuß et al.[23] and D) this work.

A detailed comparison can be found in Table S5, Supporting Information.

Reconsidering the transport model in Figure 1, critical parameters affecting the distribution between the two pathways can be derived: i) the partitioning factor of dissolved iridium between the ionomer and aqueous phase and ii) the concentration of dissolved iridium in the ionomer phase of the CL, as they control the transport rate into the aqueous phase of the CL. In turn, the concentration in the catalyst layer is dependent on the transport rate through PTL and membrane pathway. The former is affected by gas bubbles in the PTL and the operation mode of the anode water (recirculation vs. single-pass). The transport rate through the membrane is expected to change with the experiment design (full-cell vs. half-cell). Furthermore, iii) for thick CLs, the through-plane activity distribution is assumed to affect the distribution of dissolved iridium if either electric or ionic resistance starts to limit the activity and the source of dissolved iridium thus shifts toward the PTL or membrane, respectively.[50]

Based on this, the results for the distribution of dissolved iridium between the two pathways in the different electrochemical setups are qualitatively compared. Three trends can be observed:

1) *The preference for the membrane pathway is more pronounced in half-cell* (*Figure 5C,D*) *compared to full-cell experiments* (*Figure 5A,B*).Following the hypothesis that iridium dissolves in cationic and anionic form in a ratio of 80/20, in the half-cell setups a significant amount of anionic IrO_4^{2-} is transported through the membrane.[18] This can be explained by liquid electrolyte intruding into the membrane, increasing the amount of mobile ions and ionic conductivity, and thus reducing the selective inhibition of the transport of dissolved anions by migration.[42] It should also be noted that the ratio of anionic and cationic forms might vary with different catalysts and operational parameters.

Irrespective of the charge, the transport rate of dissolved ions through the membrane is increased in the half-cell setups due to:

i) ions dragged by water being transported through the membrane from the water to the electrolyte chamber by osmotic pressure.

ii) a higher diffusive flux of dissolved species resulting from the lower concentration at the cathode side of the membrane in half-cell compared to full-cell experiments. This can be explained by a higher transport rate of dissolved species from the membrane into the respective sinks, i.e., the acidic electrolyte compared to the transport into and through the CCL, and the GDL into the cathode water effluent. Due to the possibility of an exchange with protons, the partitioning factor is also expected to be shifted towards the liquid side comparing the acidic electrolyte to deionized water.[28]

iii) the formation of an Ir band over time, which inhibits transport through the membrane, especially for the larger IrO_4^{2-}.[29] As this formation is time-dependent and likely requires crossover H_2, this inhibition is not expected in the case of short-term half-cell measurements.[28] An increase in the PTL fraction over time due to this inhibition contrasts with the observed trend in this work (see Figure S5D, Supporting Information).

2) *Discrepancy in the PTL fraction within the two full-cell experiments* (*Figure 5*[17] *vs. B*[18]). At first, the derivation of the PTL

fraction relies on different assumptions in the two studies with its own limitations (see Table S5, Supporting Information). In A, it is assumed that iridium dissolves to cationic and anionic species at a ratio of 80/20, while anionic species are exclusively transported to the anode water feed. In B, the content in the membrane, CCM, and the cathode water effluent is measured separately. In particular, the determination within the membrane by scanning transmission electron microscopy-electro dispersive X-ray spectroscopy (STEM-EDXS) is not optimal for statistical analysis.

Furthermore, the discrepancy in the PTL fraction can be a result of the flow mode in the anode water cycle. While in A the electrolyzer is run in single-pass mode, in B the anode water is recirculated, leading to higher concentrations of dissolved iridium. With higher concentrations, the overall transport of the dissolved catalyst from the CL to the anode water compartment is reduced. It has been suggested that this reduction is due to the redeposition of the anionic iridium species in the CL.[29] However, the concentration observed during a recirculation phase in A is higher by one order of magnitude compared to B (see Table S5, Supporting Information), thus reducing the expected redeposition rate in B.

3) *Discrepancy in the PTL fraction within the two half-cell experiments* (*Figure 5*[28] *vs. D*). In the work by Geuß et al. (Figure 5C), a significantly higher PTL fraction (≈3%) was observed compared to this work (Figure 5D, 0.1%). In accordance with the earlier discussion, a reduction in the PTL fraction with recirculation in C compared to single-pass in D would be expected opposite to the observed trend. The effect of recirculation is, however, likely to be less pronounced considering the concentration in the anode water is two orders of magnitude lower (see Table S5, Supporting Information). Another factor that would explain the opposite trend is a higher concentration of acid in C compared to D. Higher acidity shifts the partitioning factor of dissolved catalyst species toward acidic electrolyte, and consequently, an increased transport rate of the membrane pathway could be rationalized.

In turn, the recirculation and higher acid content in C lead to the acidification of the anode compartment over time, which shifts the partitioning factor between the CL ionomer and anode water toward the liquid phase, which is one factor explaining the increased PTL fractions in C compared to D (see Table S2, Supporting Information). Another difference in the setup operation is the constant flow of the acidic electrolyte in D, while no forced convection in the electrolyte chamber is applied in C. Despite the shift in the partitioning factor of the dissolved catalyst toward the membrane due to the lower acid concentration, a steady flow of electrolyte ensures that the concentration of dissolved catalyst close to the membrane is kept to a minimum, far from the equilibrium. This, in turn, increases the diffusive flux of dissolved species through the membrane. In contrast to C, the effect of the flow rate of the anode water or the liquid electrolyte on the distribution of the PTL and the membrane pathway is relatively straightforward to investigate with the presented setup and will be part of an upcoming study.

2.4. Catalyst Dissolution with Current Density

Besides the flexibility in studying operational parameters, the influence of electrochemical and sample parameters on catalyst dissolution can be studied in a straightforward manner with the presented setup. To demonstrate this, after the conditioning hold discussed in the previous section, the dissolution during electrode polarization is recorded at various current densities and for different catalyst loadings from 0.8–1.7 mg_{Ir} cm^{-2} (see Figure S7, Supporting Information). To correlate activity and stability, the *S*-number is derived from the stabilized dissolution signal at the end of each step, and the results are displayed in **Figure 6**.

For all catalyst loadings, the *S*-number decreases by an order of magnitude with increased current. For the higher loadings, a hysteresis in the stability is observed, with a higher stability on the polarization back to a lower current density, as indicated by the direction of the marker. It should be noted that to derive the *S*-number, only the dissolution through the membrane is considered. Since at a low current density for the highest loading, some dissolution products are detected in the PTL pathway in the upward but not in the downward scan, the hysteresis presented in Figure 6 is slightly underestimated (see Figure S8, Supporting Information). The hysteresis can be explained by the progressing stabilization during the protocol and is not observed when performing a subsequent polarization curve experiment (see Figure S10, Supporting Information). However, the decrease in stability persists.

In contrast to this trend, Dam et al. observed decreasing amounts of dissolved iridium in the anode water feed with higher

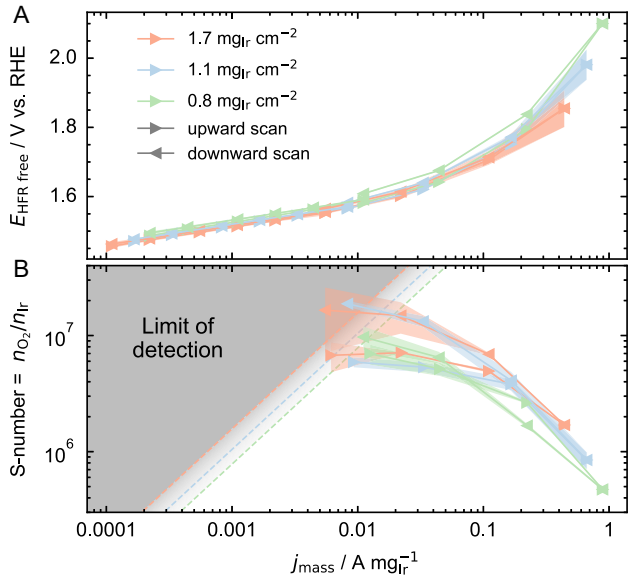

Figure 6. Activity–stability results for IrO_2/TiO_2-containing catalyst layers with different loadings at various current densities. A) Tafel plot and B) corresponding stability number derived from the integrated current and dissolution signal during the last minute of each polarization step of two independently measured samples. The shaded area depicts the minimum and maximum values of the measured samples. Only the dissolution signal through the membrane is considered. Dissolution profiles of the individual measurements are displayed in (Figure S1, Supporting Information). The dashed lines represent the detection limit for iridium of the individual measurements of 0.4–0.6 pg_{Ir} s^{-1} (see Supplementary Note 10, Supporting Information).

current densities (see Figure S11, Supporting Information).[29] Whether this observation is caused by a change in distribution between the PTL and the membrane pathway, or an actual increase in *S*-number due to another stabilizing mechanism not observed in AMSs, remains an open question. In contrast, in material-level experiments, Geiger et al. observed a proportional increase in iridium dissolution rate with the applied current and, therefore, no change in *S*-number with current density for rutile IrO_2 catalyst up to an applied current density of $1\,A\,mg_{Ir}^{-1}$ and a potential of 3 V vs. RHE (see Figure S11, Supporting Information).[23] Assuming this result for rutile IrO_2 is transferable to the catalyst used, IrO_2/TiO_2, the decrease is unlikely to be a cause of the high potential provoking another dissolution mechanism.

Instead, the observed differences in the trend of *S*-number with current density could be the result of different conditions for the catalyst in the setups utilized. With the membrane being attached to the CL, for instance, the pH and temperature at the CL, as well as the transport of dissolved iridium, are affected compared to the simpler material-level experiment (see Figure 1). A higher current density could lead to a reduction of the pH at the CL, an increase in temperature, or an increasing transport rate of dissolved iridium. The latter reduces the concentration of the dissolved species in the CL, which induces a Nernst shift of the dissolution reaction. These factors could explain the observed decrease in stability. As all of these effects are dependent on the applied geometric current density, the decrease in *S*-number should occur independently of the loading at the same geometric current density. However, the onset of the decrease in *S*-number is observed at lower geometric current densities with lower loadings (see Figure S12B, Supporting Information). In contrast, the trend in *S*-number overlaps for all loadings when plotted against mass-normalized current (Figure 6B). This suggests that the *S*-number is a function of the mass-normalized current and its decrease is dependent on the current per mass of catalyst than the current per geometric area of the catalyst layer. For temperature, which depends on the geometric current density, Geuß et al. likewise did not observe a decrease in *S*-number with applied current density and rather an increase in *S*-number with temperature (see Figure S11).[28]

A comparison of the mass- and geometric area-normalized current density also reveals that the decrease in *S*-number coincides with the deviation from the linear Tafel behavior of the HFR-free potential. Following the discussion in the previous section, inhomogeneous compression and positioning of the CE is assumed to lead to inhomogeneous current distribution across the catalyst layer and, consequently, local mass transport limitations for water and product gas and a decrease in catalyst utilization are observed even at an overall current density below $100\,mA\,cm^{-2}$. With lower loading, this effect exacerbates due to the higher in-plane resistance. Two approaches can explain the decrease in catalyst stability under mass transport limiting conditions. At first, a higher electrode potential under mass transport limitation could cause an increase in dissolution. However, this contrasts results from Geiger et al. with rutile IrO_2 as mentioned earlier. As a second explanation, the local potential is expected to change dynamically under mass transport limiting conditions. This dynamic stress could invoke transient dissolution of the catalyst and therefore the decrease in *S*-number. Further research is required to shed light on the correlation between mass transport limitations and catalyst dissolution. A causal relation between both would underline the need for a homogeneous use of the catalyst across the catalyst layer to suppress dissolution and improve CL stability when considering single-cells as well as comparing multiple cells in a stack for long-term operation.

3. Conclusions

In this study, we introduce a new method to evaluate the activity and stability of CLs for OER on a component level, bridging the gap between material- and device-level research. The two-channel electrochemical flow cell can be operated under relevant current density up to $1\,A\,cm^{-2}$. Dissolution products from the catalyst or from other cell components can be detected separately in the anode water after transport through the PTL or in the acidic electrolyte after transport through the membrane online in a resolution of seconds using ICP-MS.

For dissolved iridium catalyst, a clear preference for the membrane pathway is observed, which is even more pronounced compared to previous results on half- and full-cells. As discussed in this work, the discrepancy in distribution of dissolved species between the two pathways highlights the sensitivity of the respective transport rates on operational and material differences in the experimental setup used. As the transport rate influences the concentration in the CL and could thus affect the dissolution rate following a Nernstian shift, future research should address the question of whether the inhibition of transport can increase catalyst stability and add to the observed discrepancy between AMS and full-cell experiments. The distribution between the two pathways is therefore a crucial measurable in quantifying changes in the two transport rates.

A first study on the current density demonstrated a clear decrease in stability with higher current density. As the decrease is dependent on mass- but not geometry-normalized current, a lower stability at a high current density is related to the inhomogeneous distribution of the current within the cell and low catalyst utilization and not to the effects of transport. This highlights the importance of AMSs operating at relevant current densities to improve the understanding of discrepancies in catalyst dissolution rates in material- and device-level experiments.[26,28,51] A low material consumption and fast experimentation with a high temporal resolution make the method presented here ideal for further investigating catalyst dissolution in the catalyst layer on a component level as well as the activity and stability of next-generation catalysts for water electrolysis.

4. Experimental Section

Electrode Manufacturing

Half-side catalyst-coated membranes are prepared using the decal transfer method. CLs are made from 3 mL catalyst ink mixed in

8 mL HDPE bottles. The ink formulation consists of 1.38 g of IrO_2/TiO_2 (Elyst Ir75 0480, 75 wt% iridium, Umicore, Germany), 0.86 g ionomer dispersion (Nafion D2021, 20 wt%, Chemours, USA), and 1.6 g of a 1-propanol/H_2O solvent mixture. Taking the solvent mixture in the ionomer dispersion into account, the overall 1-propanol/H_2O ratio in the ink is 0.82 wt%. The ink solvent mixture has a solid content of 33 wt% and an ionomer/catalyst ratio of 0.131. To ensure proper ink dispersion, 8.4 g ZrO_2 beads (5 mm, Fritsch, Germany) were added, and the mixture was processed on a roller mill for 20 h at 180 rpm. The ink was then coated onto 50μm virgin PTFE using a Mayer-rod (12, 40, or 60 μm, Erichsen) at 10 mm s^{-1}. The coatings were subsequently dried at 70 °C for 3 h.

Electrodes with a 3 mm diameter are punched out and hot-pressed onto a Nafion membrane (N115, dry thickness 125 μm, Chemours, USA) at 155 °C and 2.5 MPa for 4 min using a high-performance press (Lab·Line P200S, COLLIN Lab & Pilot Solutions GmbH, Germany). To this end, the CL and membrane are placed between Kapton foil (CMC Klebetechnik, Germany) and pressure equalization pads (PacoPads, Pacothane Technologies, USA) to protect against impurities being hot-pressed into the membrane and to compensate for height inhomogeneities along the compressed area, respectively. The loading of the coating is determined by weighing the decal PTFE with and without the CL (±0.001 mg, Sartorius Cubis, Germany).

Electrochemical Measurements

The setup illustrated in Figure 2 was used. The bottom flow cell was milled from titanium (Grade 1, E. Wagener). The top flow cell was 3D-printed by stereolithography (Formlabs Form 3+, Clear V4 resin). Both had a channel width of 2 mm and an opening angle of 60°. A Ti fiber sinter material (2GDL40-1.0, 56% porosity, 1 mm thickness, NV Bekaert SA, Belgium) was used as a PTL and laser cut to an elliptical shape (2.5/2.8 mm diameter). The sealing ring around the PTL is made from two-component silicone (SF45—RTV2, Silikonfabrik, Germany) using a 3D-printed negative mold and cured overnight at room temperature. A gas diffusion layer (H23C8, Freudenberg, Germany) was used as a CE, which was hot-pressed onto a Nafion membrane in accordance with the procedure for the iridium CL but with a reduced pressure of 1.2 MPa. The CE was contacted by a glassy carbon rod (∅3 mm, Sigradur G, HTW Hochtemperatur Werkstoffe, Germany). Sealing rings around the CE were punched out from EPDM rubber sheets (1/32″ & 1/64″ thickness, McMASTER-CARR, USA). Potentials were referenced against a reversible hydrogen electrode (RHE, Mini-Hydroflex, Gaskatel, Germany) connected via the membrane and a separate electrolyte channel to the WE (see Figure 2C).

At the start of each experiment day, sealing rings, flow cells, and the PTL were cleaned in isopropanol and DI water in an ultrasonic bath in both solvents for 10 min each. The bottom flow cell was then mounted onto XYZ translational stages (M-403.6DG, Physik Instrumente, Germany), and the PTL with its sealing ring was inserted. After assembling the CE compartment, the top flow cell was mounted above the stages onto a double-bending beam force sensor (KD45 50N/VA, ME-Meßsysteme, Germany), as displayed in (Figure S13, Supporting Information). The alignment of the two flow cells, and with it a homogeneous compression at the edge of the PTL, was verified by clamping pressure-sensitive paper (Super Low Pressure (LLW), Prescale, Fujifilm Europe GmbH, Germany) between the cells (see Figure S1, Supporting Information). The top flow cell was filled and continuously pumped with Ar-purged 0.1 M $HClO_4$ prepared from the concentrated acid (Suprapur, 70%, Merck, Germany) and ultrapure water (>18 MΩ cm, Milli-Q, Merck, Germany). Ar-purged ultrapure water was used for the bottom flow cell.

A h-CCM with the membrane facing upwards was manually positioned on top of the PTL. The bottom flow cell along with the sample was approached toward the top flow cell having a hanging meniscus from the main channel and the RE compartment. The cells were compressed with 20throughout the experiment by controlling the *Z*-axis position over time. The electrochemical procedure was applied using a Gamry Reference 620 (Gamry Instruments, USA). Details of the protocol are outlined in (Table S6, Supporting Information). During operation, evolved oxygen from the WE was removed by a microfluidic bubble trap (Darwin microfluidics, Elveflow, France) using a membrane pump (VWR International, USA). Measurements were performed at room temperature.

ICP-MS Measurements

Either the outlet of the top flow cell (referred to as through the membrane) or the bottom cell (referred to as through the PTL) was connected to an ICP-MS (Agilent 7900, Agilent Technologies, USA). Prior to this, calibration was performed with standard solutions (Certipur ICP-MS Standard, Merck, Germany). The flow rate of liquid from the cell to the ICP-MS was measured daily. Before being introduced to the ICP-MS, the analyte liquid was mixed with an internal standard with a concentration of 3 μg_{Re} L^{-1} and 2 μg_{Sc} L^{-1}. The signal for $m/z = 45$ (Sc), 47 (Ti), 187 (Re), and 193 (Ir) was recorded continuously. The dissolution signal is shifted in time to account for the delay due to mass transport from electrochemical cell to ICP-MS which is in between 10 to 20 s. The signal of the internal standard is fitted with a linear model to reduce noise in the calibrated signal. Data processing, analysis and visualization is perfomed using a research data management system previously described, all routines are made available online.[52]

Acknowledgements

N.C.R. and D.D. gratefully acknowledge the funding by the German Federal Ministry of Education and Research (BMBF) within the project 03HY108A. J.Z. acknowledges financial support from the European Union under ERC Synergy Grant DEMI, GA no. 101118768. L.L. would like to thank the German Federal Ministry for Economic Affairs and Energy (BMWi) for the financial support within the framework of the HoKaWe project (BMWi/03EI3029A).

Open Access funding enabled and organized by Projekt DEAL.

Conflict of Interest

The authors declare no conflict of interest.

Author Contributions

Nico C. Röttcher: conceptualization (lead); data curation (lead); formal analysis (lead); investigation (lead); methodology (lead); software (lead); validation (lead); visualization (lead); writing—original draft (lead). **Jiahua Zhou**: formal analysis (supporting); methodology (supporting); software (supporting); writing—review & editing (equal). **Lukas Löttert**: resources (supporting); writing—review & editing (equal). **Karl J. J. Mayrhofer**: conceptualization (supporting); funding acquisition (lead); resources (lead); supervision (supporting); writing—review & editing (equal). **Dominik Dworschak**: conceptualization (supporting);

methodology (supporting); project administration (lead); supervision (lead); writing—review & editing (equal).

Data Availability Statement

Raw data and analysis as well as visualization routines are made available, here https://zenodo.org/records/15230541. As presented in a previous publication, raw data are structured in an SQLite database file; Jupyter notebooks are created for data analysis and visualization, and can be interactively executed online with Binder.

Keywords: high-current operation · high-throughput screening · iridium dissolution · online ICP-MS · water electrolysis

[1] K. Ayers, N. Danilovic, R. Ouimet, M. Carmo, B. Pivovar, M. Bornstein, *Annu. Rev. Chem. Biomol. Eng.* **2019**, *10*, 219.
[2] U. Babic, M. Suermann, F. N. Büchi, L. Gubler, T. J. Schmidt, *J. Electrochem. Soc.* **2017**, *164*, 387.
[3] C. Minke, M. Suermann, B. Bensmann, R. Hanke-Rauschenbach, *Int. J. Hydrogen Energy* **2021**, *46*, 23581.
[4] S. Kiemel, T. Smolinka, F. Lehner, J. Full, A. Sauer, R. Miehe, *Int. J. Energy Res.* **2021**, *45*, 9914.
[5] M. Clapp, C. M. Zalitis, M. Ryan, *Catal. Today* **2023**, *420*, 114140.
[6] C. Wang, K. Lee, C. P. Liu, D. Kulkarni, P. Atanassov, X. Peng, I. V. Zenyuk, *Int. Mater. Rev.* **2024**, *69*, 3.
[7] H. Yu, N. Danilovic, Y. Wang, W. Willis, A. Poozhikunnath, L. Bonville, C. Capuano, K. Ayers, R. Maric, *Appl. Catal. B: Environ.* **2018**, *239*, 133.
[8] Z. Taie, X. Peng, D. Kulkarni, I. V. Zenyuk, A. Z. Weber, C. Hagen, N. Danilovic, *ACS Appl. Mater. Interfaces* **2020**, *12*, 52701.
[9] J. K. Lee, G. Anderson, A. W. Tricker, F. Babbe, A. Madan, D. A. Cullen, J. D. Arregui-Mena, N. Danilovic, R. Mukundan, A. Z. Weber, X. Peng, *Nat. Commun.* **2023**, *14*, 4592.
[10] H. Yu, L. Bonville, J. Jankovic, R. Maric, *Appl. Catal. B: Environ.* **2020**, *260*, 118194.
[11] S. M. Alia, S. Stariha, R. L. Borup, *J. Electrochem. Soc.* **2019**, *166*, F1164.
[12] J. Murawski, S. Scott, R. Rao, K. Rigg, C. Zalitis, J. Stevens, J. Sharman, G. Hinds, I. E. Stephens, *Johnson Matthey Technol. Rev.* **2023**, *68*, 121.
[13] A. Weiß, A. Siebel, M. Bernt, T.-H. Shen, V. Tileli, H. A. Gasteiger, *J. Electrochem. Soc.* **2019**, *166*, F487.
[14] S. M. Alia, K. S. Reeves, D. A. Cullen, H. Yu, A. J. Kropf, N. Kariuki, J. H. Park, D. J. Myers, *J. Electrochem. Soc.* **2024**, *171*, 044503.
[15] S. O. Klemm, A. A. Topalov, C. A. Laska, K. J. Mayrhofer, *Electrochem. Commun.* **2011**, *13*, 1533.
[16] A. K. Schuppert, A. A. Topalov, I. Katsounaros, S. O. Klemm, K. J. J. Mayrhofer, *J. Electrochem. Soc.* **2012**, *159*, 670.
[17] M. Milosevic, T. Böhm, A. Körner, M. Bierling, L. Winkelmann, K. Ehelebe, A. Hutzler, M. Suermann, S. Thiele, S. Cherevko, *ACS Energy Lett.* **2023**, *8*, 2682.
[18] A. P. Dam, B. Y. A. Abuthaher, G. Papakonstantinou, K. Sundmacher, *J. Electrochem. Soc.* **2023**, *170*, 064504.
[19] Z. Zeng, R. Ouimet, L. Bonville, A. Niedzwiecki, C. Capuano, K. Ayers, A. P. Soleymani, J. Jankovic, H. Yu, G. Mirshekari, R. Maric, S. Bliznakov, *J. Electrochem. Soc.* **2022**, *169*, 054536.
[20] C. Wei, Z. Wang, K. Otani, D. Hochfilzer, K. Zhang, R. Nielsen, I. Chorkendorff, J. Kibsgaard, *ACS Catal.* **2023**, *13*, 14058.
[21] A. E. Thorarinsdottir, S. S. Veroneau, D. G. Nocera, *Nat. Commun.* **2022**, *13*, 1243.
[22] M. Zlatar, D. Escalera-López, M. G. Rodríguez, T. Hrbek, C. Götz, R. Mary Joy, A. Savan, H. P. Tran, H. N. Nong, P. Pobedinskas, V. Briega-Martos, A. Hutzler, T. Böhm, K. Haenen, A. Ludwig, I. Khalakhan, P. Strasser, S. Cherevko, *ACS Catal.* **2023**, *13*, 15375.
[23] S. Geiger, O. Kasian, M. Ledendecker, E. Pizzutilo, A. M. Mingers, W. T. Fu, O. Diaz-Morales, Z. Li, T. Oellers, L. Fruchter, A. Ludwig, K. J. J. Mayrhofer, M. T. M. Koper, S. Cherevko, *Nat. Catal.* **2018**, *1*, 508.
[24] O. Kasian, J.-P. Grote, S. Geiger, S. Cherevko, K. J. J. Mayrhofer, *Angew. Chem. Int. Ed.* **2018**, *57*, 2488.
[25] J. Zhu, L. Li, M. Cao, *Nano Energy* **2024**, *122*, 109300.
[26] J. Knöppel, M. Möckl, D. Escalera-López, K. Stojanovski, M. Bierling, T. Böhm, S. Thiele, M. Rzepka, S. Cherevko, *Nat. Commun.* **2021**, *12*, 2231.
[27] K. Ehelebe, J. Knöppel, M. Bierling, B. Mayerhöfer, T. Böhm, N. Kulyk, S. Thiele, K. Mayrhofer, S. Cherevko, *Angew. Chem. Int. Ed.* **2021**, *60*, 8882.
[28] M. Geuß, L. Löttert, T. Böhm, A. Hutzler, K. J. J. Mayrhofer, S. Thiele, S. Cherevko, *ACS Catal.* **2024**, *14*, 11819.
[29] A. P. Dam, T. Franz, G. Papakonstantinou, K. Sundmacher, *Appl. Catal. B: Environ.* **2025**, *365*, 124946.
[30] S. Geiger, O. Kasian, A. M. Mingers, S. S. Nicley, K. Haenen, K. J. J. Mayrhofer, S. Cherevko, *ChemSusChem* **2017**, *10*, 4140.
[31] A. Bornet, P. Moreno-García, A. Dutta, Y. Kong, M. Liechti, S. Vesztergom, M. Arenz, P. Broekmann, *ACS Catal.* **2024**, *14*, 17331.
[32] J. Schröder, V. A. Mints, A. Bornet, E. Berner, M. Fathi Tovini, J. Quinson, G. K. H. Wiberg, F. Bizzotto, H. A. El-Sayed, M. Arenz, *JACS Au* **2021**, *1*, 247.
[33] M. Geuß, M. Milosevic, M. Bierling, L. Löttert, D. Abbas, D. Escalera-López, V. Lloret, K. Ehelebe, K. J. J. Mayrhofer, S. Thiele, S. Cherevko, *J. Electrochem. Soc.* **2023**, *170*, 114510.
[34] K. Ehelebe, D. Seeberger, M. T. Y. Paul, S. Thiele, K. J. J. Mayrhofer, S. Cherevko, *J. Electrochem. Soc.* **2019**, *166*, F1259.
[35] M. Inaba, A. W. Jensen, G. W. Sievers, M. Escudero-Escribano, A. Zana, M. Arenz, *Energy Environ. Sci.* **2018**, *11*, 988.
[36] P. C. Jiménez, G. K. H. Wiberg, G. W. Sievers, V. Brüser, M. Arenz, *J. Mater. Chem. A* **2023**, *11*, 20129.
[37] A. Steinbach, M. Ulsh, H. Xi, *Low-Cost, High Performance Catalyst Coated Membranes for PEM Water Electrolyzers, Technical Report DOE-3M-0008425*, U.S. Department of Energy, United States **2022**.
[38] I. Reichmann, V. Lloret, K. Ehelebe, P. Lauf, K. Jenewein, K. J. J. Mayrhofer, S. Cherevko, *ACS Meas. Sci. Au* **2024**, *4*, 515.
[39] L. Fiedler, T.-C. Ma, B. Fritsch, J. H. Risse, M. Lechner, D. Dworschak, M. Merklein, K. J. J. Mayrhofer, A. Hutzler, *ChemElectroChem* **2023**, *10*, e202300373.
[40] G. Papakonstantinou, G. Algara-Siller, D. Teschner, T. Vidakovic′-Koch, R. Schlögl, K. Sundmacher, *Appl. Energy* **2020**, *280*, 115911.
[41] R. Sander, *Atmos. Chem. Phys.* **2015**, *15*, 4399.
[42] H. T. B. Ngo, Y. J. Jo, W. Kim, H. An, H. B. Park, H. W. Kim, *Polymer* **2024**, *305*, 127180.
[43] B. D. Bath, H. S. White, E. R. Scott, *Anal. Chem.* **2000**, *72*, 433.
[44] G. K. Wiberg, S. Nösberger, M. Arenz, *Curr. Opin. Electrochem.* **2022**, *36*, 101129.
[45] A. J. McLeod, L. V. Bühre, B. Bensmann, O. E. Herrera, W. Mérida, *J. Power Sources* **2024**, *589*, 233750.
[46] P. K. Giesbrecht, M. S. Freund, *ACS Appl. Energy Mater.* **2024**, *7*, 7272.
[47] M. Bernt, H. A. Gasteiger, *J. Electrochem. Soc.* **2016**, *163*, 3179.
[48] C. C. Weber, J. A. Wrubel, L. Gubler, G. Bender, S. Angelis, F. N. Büchi, *ACS Appl. Mater. Interfaces* **2023**, *15*, 34750.
[49] C. van Pham, M. Bühler, J. Knöppel, M. Bierling, D. Seeberger, D. Escalera-López, K. J. Mayrhofer, S. Cherevko, S. Thiele, *Appl. Catal. B Environ.* **2020**, *269*, 118762.
[50] E. Padgett, G. Bender, A. Haug, K. Lewinski, F. Sun, H. Yu, D. A. Cullen, A. J. Steinbach, S. M. Alia, *J. Electrochem. Soc.* **2023**, *170*, 084512.
[51] K. Ehelebe, D. Escalera-López, S. Cherevko, *Curr. Opin. Electrochem.* **2021**, *29*, 100832.
[52] N. C. Röttcher, G. D. Akkoç, S. Finger, B. Fritsch, J. Möller, K. Mayrhofer, D. Dworschak, *J. Mater. Chem. A* **2024**, *12*, 3933.

Manuscript received: March 11, 2025
Revised manuscript received: April 16, 2025
Version of record online: May 12, 2025